Jupiter's ion radiation belts inward of Europa's orbit

Peter Kollmann[1], George Clark[2], Christopher P. Paranicas[3], Barry H. Mauk[3], Elias Roussos[4], Quentin Nénon[5], Henry Berry Garrett[6], Angélica Sicard[7], Dennis K Haggerty[2], and Abigail Mary Rymer[8]

[1]The Johns Hopkins University Applied Physics Laboratory
[2]Johns Hopkins University Applied Physics Laboratory
[3]Johns Hopkins University
[4]Max Planck Institute for Solar System Research
[5]University of California, Berkeley
[6]California Institute of Technology
[7]ONERA, the French Aerospace Lab
[8]Johns Hopkins Applied Physics Laboratory

November 25, 2022

Abstract

Jupiter is surrounded by intense and energetic radiation belts, yet most of the available in-situ data, in volume and quality, were taken outside of Europa's orbit, where radiation conditions are not that extreme. Here we study measurements of ions of tens of keV to tens of MeV at <10 Jupiter radii (RJ) distance to Jupiter, therefore inward of the orbit of Europa. Ion intensities drop around 6RJ, near Io's orbit. Previous missions reported on radiation belts of tens and hundreds of MeV ions located between 2 and 4 RJ. Measurements of lower energies were not conclusive because high energy particles typically contaminate the measurement of lower energy particles. Here we show for the first time that ions in the hundreds of keV range are present and suggest that ions may extend even into the GeV range. The observation of charged particles yields information on the entire field line, not just the local field. We find that there is a region close to Jupiter where no magnetic trapping is possible. Jupiter's innermost radiation belt is located at <2RJ, inward of the main ring. Previous work suggested that this belt is sourced by reionized energetic neutral atoms coming steadily inward from distant regions. Here we perform a phase space density analysis that shows consistency with such a local source. However, an alternative explanation is that the radiation belt is populated by occasional strong radial transport and then decays on the timescale of years.

Jupiter's ion radiation belts inward of Europa's orbit

P. Kollmann[1], G. Clark[1], C. Paranicas[1], B. Mauk[1], E. Roussos[2], Q. Nénon[3], H. B. Garrett[4],

A. Sicard[5], D. Haggerty[1], A. Rymer[1]

[1] Johns Hopkins University Applied Physics Laboratory, Laurel, MD 20723-6099, USA

[2] Max Planck Institute for Solar System Research, 37077 Göttingen, Germany

[3] Space Sciences Laboratory, University of California at Berkeley, Berkeley CA, USA

[4] NASA Jet Propulsion Laboratory, California Institute of Technology, Pasadena, CA, USA

[5] ONERA, The French Aerospace Lab, Toulouse, France

Abstract

Jupiter is surrounded by intense and energetic radiation belts, yet most of the available in-situ data, in volume and quality, were taken outside of Europa's orbit, where radiation conditions are not that extreme. Here we study measurements of ions of tens of keV to tens of MeV at < 10 Jupiter radii (R_J) distance to Jupiter, therefore inward of the orbit of Europa. Ion intensities drop around $6R_J$, near Io's orbit. Previous missions reported on radiation belts of tens and hundreds of MeV ions located between 2 and $4R_J$. Measurements of lower energies were not conclusive because high energy particles typically contaminate the measurement of lower energy particles. Here we show for the first time that ions in the hundreds of keV range are present and suggest that ions may extend even into the GeV range. The observation of charged particles yields information on the entire field line, not just the local field. We find that there is a region close to Jupiter where no magnetic trapping is possible. Jupiter's innermost radiation belt is located at $< 2R_J$, inward of the main ring. Previous work suggested that this belt is sourced by reionized energetic neutral atoms coming steadily inward from distant regions. Here we perform a phase space density analysis that shows consistency with such a local source. However, an alternative explanation is that the radiation belt is populated by occasional strong radial transport and then decays on the timescale of years.

Plain Language Summary

Planets with a magnetic field, like Earth and Jupiter, are surrounded by belts of natural charged particle radiation. Some of the most extreme radiation conditions are found at Jupiter, which makes this planet an ideal laboratory to study how radiation is building up in space. Even though raw measurements from satellites in orbit of Jupiter exists, they often cannot be used as-is. This is because strong enough radiation interferes with radiation instruments similarly as direct sunlight interferes with a thermometer. Here we present results of a careful processing of data from the Juno mission to get around the instrument limitations. We are for the first time able to measure ions in an energy range that was not unambiguously measured before. Such measurements are the basis for trying to understand how these radiation belts are forming. We use this to study the origin of the radiation belt closest to Jupiter. Our results on this topic are not conclusive yet but one possibility is that this belt may be made from ions that originate from larger distances around Jupiter.

Key Points:

- Ion belts at 2-4 Jovian radii distance have significant intensities from hundreds of keV to GeV

- Phase space densities of the innermost ion belt suggest non-steady state or local source

- A region without stable trapping exists close to Jupiter

1 Introduction

Jupiter has the largest magnetosphere in the solar system and the most energetic electron radiation belts [*Mauk and Fox*, 2010; *Roussos and Kollmann*, 2020]. It has been visited by several spacecraft [*Krupp et al.*, 2004], yet there are regions in space and particle energy that are not well explored [*Roussos et al.*, 2019]. Reliable in-situ radiation measurements are particularly rare inward of the orbit of Io because the intensity of the electron radiation belt becomes so intense that it interferes with the measurements even of instruments designed to measure radiation [*Mauk et al.*, 2016; *Kollmann et al.*, 2020a]. Both electrons and very energetic ion radiation belts cause interference (Sec. 3, *Nénon et al.* [2018a]). Here we carefully analyze the Juno/JEDI data (Sec. 2.1) to pick out reliable measurements despite the contamination by radiation (Sec. 3). We use that data to study the physics of the innermost radiation belt (Sec. 4).

1.1 From Europa to the Main Ring

The differential intensity (particles per time, area, solid angle, and energy interval) of energetic ions and electrons is continuously rising from the outer magnetosphere, across the orbit of Europa (at a distance of $9.4R_J$ to Jupiter with Jupiter radius=$1R_J$) until the orbit of Io ($5.9R_J$) (Fig. 2, *Kollmann et al.* [2018a]). We will refer to that region outward of Io as the "outer" radiation belt. The Europa gas torus has a subtle effect (depletion by factor < 2) on ions with pitch angles of $70°$ [*Kollmann et al.*, 2016; *Nénon and André*, 2019] because it charge exchanges with ions. This effect of Europa is barely noticeable in the mission-averaged radial intensity distribution (Fig. 2, *Kollmann et al.* [2018a, 2020a]). (Comparing non-consecutive measurements may give a different impression [*Mauk et al.*, 2004] because intensities in Jupiter's magnetosphere easily vary by an order of magnitude [*Kollmann et al.*, 2018a].)

Intensities are decreasing toward the orbit of Io. The effect is strong for protons (decrease by factor ≈ 100) and weak for electrons (factor ≈ 2). The loss is thought to be mostly due

to wave-particle interactions that scatter the particles into the atmospheric loss cone. Electrons scatter with whistler mode chorus and hiss waves *Nénon et al.* [2017] and protons with electromagnetic ion cyclotron waves *Nénon et al.* [2018b]. Other waves may generally play roles in scattering and acceleration [*Menietti et al.*, 2012].

Several discrete ion radiation belts are found roughly in the region between 2 and 4 R_J (Fig. 1). They are separated by the minor moons Amalthea ($2.5R_J$) and Thebe ($3.1R_J$). We will refer to them as the "middle" belts. All potentially reliable ion measurements we are aware of are at tens and hundreds of MeV [*Fillius et al.*, 1975; *Nénon et al.*, 2018a; *Roussos et al.*, 2019]. Juno/JEDI measures lower energies, nominally in the keV to tens of MeV range. Early Juno measurements suggested that there are no ions within this energy range associated with the middle radiation belts [*Kollmann et al.*, 2018b]. This would be peculiar as ion spectra usually show strong low energy populations. However, the original Juno observations suffered an observational bias (Appendix E) and we are now able to present reliable low energy ion measurements also in the middle belts (Sec. 3).

1.2 From Main Ring to Planet

Jupiter's innermost ion radiation belt is located inward of the Main Ring ($1.8R_J$). This belt is likely losing particles to the ionosphere [*Valek et al.*, 2020] and to some low extent also to the Main Ring *Nénon et al.* [2018a], requiring it to be replenished with particles at least occasionally. CRAND (cosmic ray albedo neutron decay) is a common source of energetic protons close to Earth and Saturn [*Cooper and Sturner*, 2018] but it is likely not important in the innermost radiation belt as this belt includes significant intensities of heavier ions [*Kollmann et al.*, 2017; *Nénon et al.*, 2018a] that cannot derive from CRAND. [*Kollmann et al.*, 2017] therefore suggested that the innermost belt is supplied through the stripping of energetic neutral atoms (ENAs) that are produced in the magnetosphere [*Mauk et al.*, 2020], a portion of which rain continuously down onto the planet. This process is also working at the Earth [*Gusev et al.*, 2003; *Petrov et al.*, 2009; *LLera et al.*, 2017] and Saturn [*Krimigis et al.*, 2005; *Krupp et al.*, 2018]. However, at these planets the process only leads to an extension of the existing radiation belts. It is not proven yet whether this process is indeed able to yield a full standalone radiation belt. We discuss this possibility in Sec. 4.3.

Overall, the nature of the innermost radiation belt and several of its properties have remained elusive so far. Even determining its precise location has proven to be difficult due Jupiter's
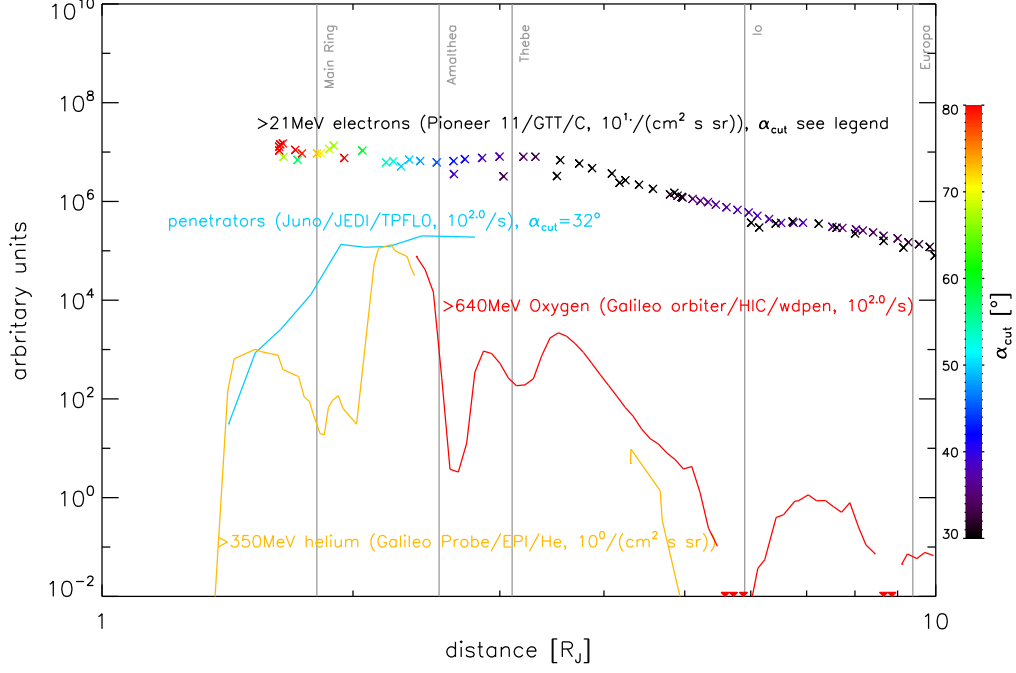
Figure 1. Distribution of energetic particles inward of Europa's orbit from Juno and earlier missions.
Orange: Measurements by Galileo Probe/EPI [*Fischer et al.*, 1996]. Its "He" channel measures $>$ 350MeV
helium ions [*Nénon et al.*, 2018b]. Red: Mission-averaged measurements by Galileo orbiter/HIC [*Roussos
et al.*, 2019]. The "wdpen" channel measures $Z \geq$ 6 ions with 50-80MeV/nuc [*Garrett et al.*, 2011]. Col-
ored "x"-symbols: Measurements by Pioneer 11/GTT. Its C detector measured in the Jupiter environment
mostly $>$ 21MeV electrons [*Baker and van Allen*, 1976]. Distances are calculated in the same field model
as Juno data. Colors code α_{cut} (see Sec. 2.3). Cyan: Mission-averaged measurements by Juno/JEDI. Its
"TPF0" channel is likely dominated by $>$ 3GeV protons close to Jupiter (Sec. 3.2). Only measurements with
$alpha_{cut} \approx 32°$ are selected.

high-order magnetic field configuration. Significant progress has been made on developing a precise magnetic field model [*Connerney et al.*, 2018]. We will show in Sec. 4.1 that this model allows us to reproduce features in the data unexplainable with older models. However, we show that even with this new model we cannot completely fit the particle data.

2 Data set

2.1 JEDI

Most data used in this study was acquired by the JEDI instrument (Jupiter Energetic Particle Detector Instrument) that nominally measures ions in the tens of keV to tens of MeV range [*Mauk et al.*, 2013] as well as electrons in the tens of keV to hundreds of keV range. Even though JEDI was not designed for this, it also shows sensitivity to higher energy particles, which we discuss and leverage in Sec. 3.2. JEDI measures particles through their energy deposited in solid state detectors (SSDs) and distinguishes high energy ion species through simultaneous measurement of their time of flight (TOF) within the instrument. Electrons are detected through SSDs with a flashing that is no significant blockade for electrons but requires at least 250keV protons to penetrate. We discuss some more of JEDI's technical details in Appendix A.

Oxygen and sulfur are only distinguished in the middle of JEDI's energy range. Depending on the used data product, we will either calculate an estimate of the pure oxygen intensities over the full energy range (Appendix D) or sum oxygen and sulfur counts together and refer to them as "heavy" ions (Appendix B).

JEDI was operating at the beginning of the mission without its TOF system at closest approach for safety reasons. When it is necessary to show measurements for single orbits at closest approach, we use SSD-only measurements that use JEDI's large, unflashed SSDs. These counts are dominated by keV ions in the innermost belt [*Kollmann et al.*, 2017] and GeV penetrators in the middle belts (Sec. 3.2). Because of this ambiguity on particle species, we will refer to these as "total particle measurements".

2.2 Other radiation measurements

We set the JEDI data in context with data from previous missions. Many instruments saturate in the high intensity environment near Jupiter. We use a version of data from the Pi-

oneer 11/GTT instrument (University of Iowa Geiger Tube Counter) [*Van Allen et al.*, 1974] that were corrected for dead time as described in Appendix F.

Also Galileo Probe/EPI measurements saturated near the planet. We use corrected values from *Pehlke* [2000]. Note that several other EPI channels that are not used here are contaminated by electrons and helium ions *Nénon et al.* [2018b,a].

2.3 Magnetic coordinates

We organize the data based on the JRM09 magnetic field model [*Connerney et al.*, 2018] combined with the "CAN" current sheet model [*Connerney et al.*, 1981].

We organize the data in M-shell, which is the radial distance of minimum magnetic field on the respective field line to Jupiter's center. This quantity is sometimes referred to as magnetic distance. M-shell is identical to L-shell only in a dipole field. We refer to the area of minimum magnetic field along all field lines as the magnetic equator.

The equatorial pitch angle of the edge of the loss cone α_l is calculated from the magnetic field B_l where the field line enters the oblate planetary surface and the field B_{eq} at the magnetic equator, where the field reaches its minimum.

$$\alpha_l = asin(\sqrt{B_{eq}/B_l}) \tag{1}$$

Northern and southern loss cone angles are generally different. Unless not explicitly mentioned we will refer to "the" loss cone angle as the maximum value of north and south.

A quantity that is useful to calculate for missions in polar orbits is the maximum observable equatorial pitch angle α_{cut} at a respective latitude. As equatorially mirroring particles do not reach higher latitudes α_{cut} is only $90°$ at the magnetic equator and smaller otherwise. α_{cut} is therefore a measure of magnetic latitude that can be immediately compared to pitch angle distributions.

3 Middle Radiation Belts

This section covers the radiation belts located between the Main Ring and Io that show their highest intensities at $2 \lesssim M \lesssim 4$. Data from earlier missions suggest that Amalthea and Thebe split this region into 3 belts (Fig. 1). We do not make this distinction here because it will turn out that our analysis currently cannot resolve this structure (Fig. 2).

3.1 Hundreds of keV ions

It can happen that particle instruments misidentify the species or energy of the particles they are counting. This happens for example in environments with high intensities of high energy particles that can reach the detectors by penetrating through the shielding of the instrument instead by entering through the aperture in the desired way. Measured intensities often appear higher in such cases than they actually are.

The region inward of Io is known to cause such problems in most instruments, including many measurements of Galileo orbiter/EPD [*Kollmann et al.*, 2018a, 2020a] and Galileo Probe/EPI [*Nénon et al.*, 2018b,a]. JEDI has the same issues in principle but some measurements are accurate because the contamination varies with latitude and possibly time. Thanks to JEDI's good pitch angle coverage, and the downlink of event data that is good for diagnostic, we are able to identify and remove contaminated parts (Appendix A and C).

Figure 2 shows mission-averaged intensities of cleaned protons and oxygen ions. Note that the equatorial pitch angle coverage changes with distance to the planet and that only measurements at small M-shells include near-equatorially mirroring particles. Because equatorial particles typically show the highest intensities, the intensities shown in Fig. 2 may appear to rise faster toward the planet than intensities at constant pitch angle. Appendix C details on how the data were cleaned and Appendix D on how the mission average was computed. Fluctuations in the mission-average profiles arise because every orbit covers a different equatorial pitch angle range and that not every pitch angle is evenly sampled. These limitations introduce noise in the mission-average profiles, which is why the actual profiles are likely much more smooth than those we show.

Figure 1 shows that there are proton radiation belts outward of the main ring and an oxygen belt at least outside of Amalthea's orbit. These radiation belts include $< 1\text{MeV}$ ions. Earlier measurements were all limited to much higher energies. This is the first time that such low energy ions are unambiguously identified in this region and allowing us to provide energy resolved spectra.

JEDI's standard data product splits proton spectra into 24 and heavy ions into 15 predefined energy steps called "rate channels". These channels therefore have a coarse energy resolution and cover a smaller energy range than what the instrument is able to measure. Because of this we use of another data product called "event data" that is downlinked with the much
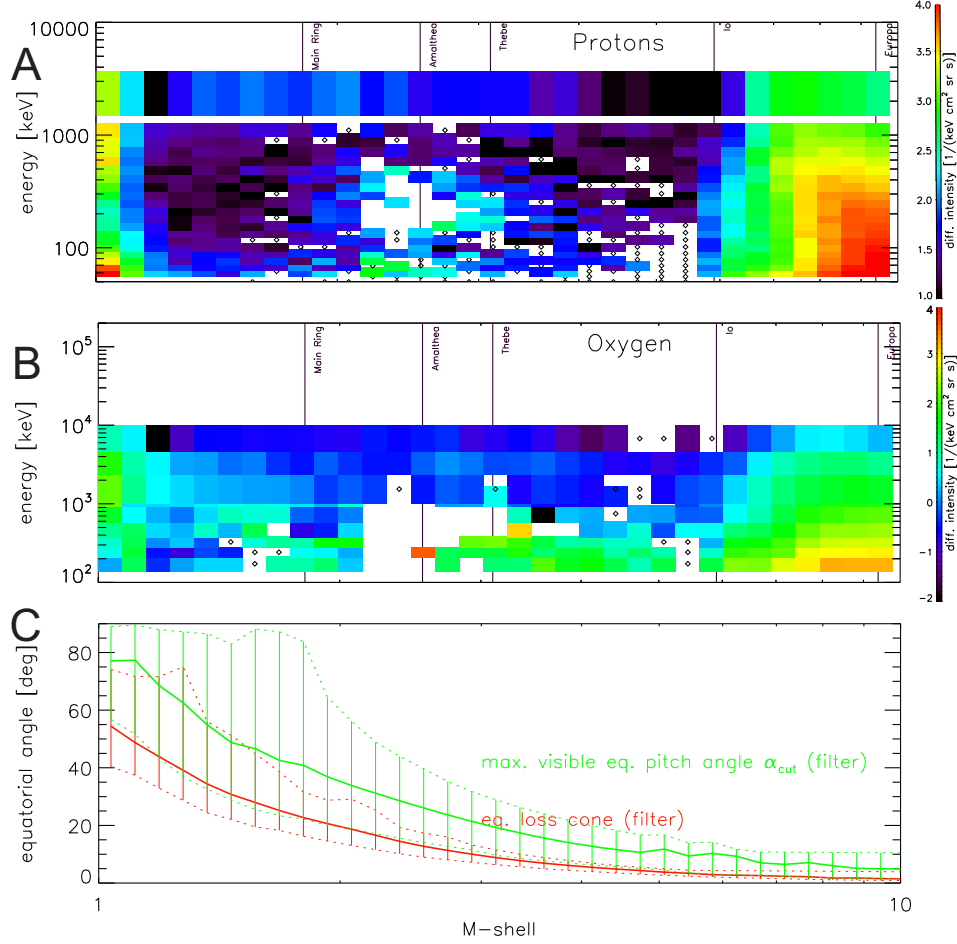
Figure 2. Mission-averaged intensities of 45keV-3.6MeV protons (panel A) and 140keV-8MeV oxygen

ions (panel B) as a function of M-shell (Sec. 2.3). Penetrating particle contamination was removed (see Ap-

pendix C). We only consider measurements with local pitch angles of 80 $-$ 90°. Panel C: The pitch angle

coverage is systematically changing with distance to the planet. The green curve shows the maximum visible

equatorial pitch angle α_{cut} and red shows the loss cone angle. Center values are mission averages; error bars

show the most extreme values covered by all orbits.

higher native resolution and the full energy range. We use event data to provide high resolution spectra shown in Fig. 3. The price of using this data is that it complicates analysis (Appendix B) and lowers the possible time resolution because only a subset of counts is recorded like this.
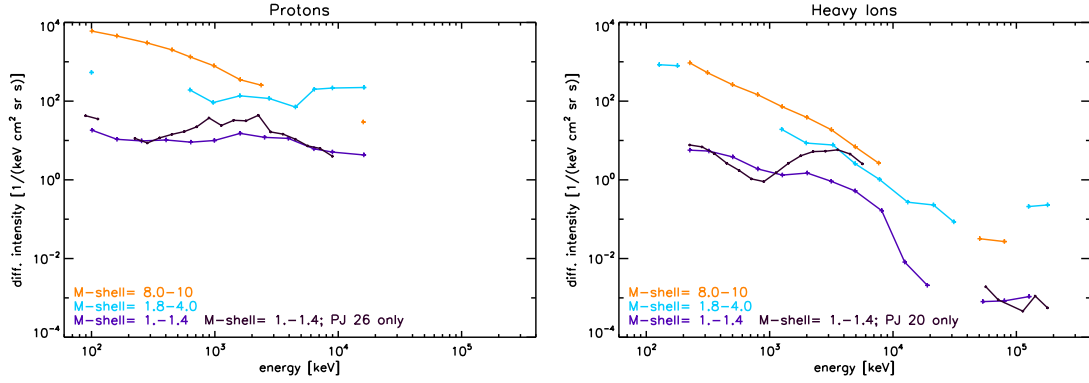

Figure 3. Energy spectra of protons (left) and heavy ions (right) in the outer belt outward of Io (orange), the middle radiation belts (cyan), and the innermost belt (violet and black). All data are mission averages except the black curve that is for a single orbit. M-shell values and orbit numbers are given in the legend.

Figure 3 illustrates that JEDI measures significant intensities of protons up to $\approx 20\text{MeV}$ and heavies up to $\approx 200\text{MeV}$. More energetic particles likely exist and may range to GeV energies (see following Sec. 3.2) but JEDI does not have the TOF resolution and detection efficiency to unambiguously identify them (Appendix B).

Proton spectra in the middle belts (as well as and the innermost belt discussed more in Sec. 4) are lower intensity but harder than what is found outside of Io. The middle belt proton intensity in the hundreds of keV range is lower than in the outer belt. *Nénon et al.* [2018b] suggested that $\lesssim 10\text{MeV}$ protons suffer strong losses at Io's orbit because they are scattered by EMIC waves into the loss cone. This mechanism results in modeled middle belt proton spectra that are flat at these energies, similar to what we are observing.

Heavy ion spectra in the middle belts ($2 \lesssim M \lesssim 4$) are similar to what is found outside of Io (except for around 100MeV). This observation suggests that EMIC wave scattering is far less efficient for these heavy ions, at least in the energy range considered here.
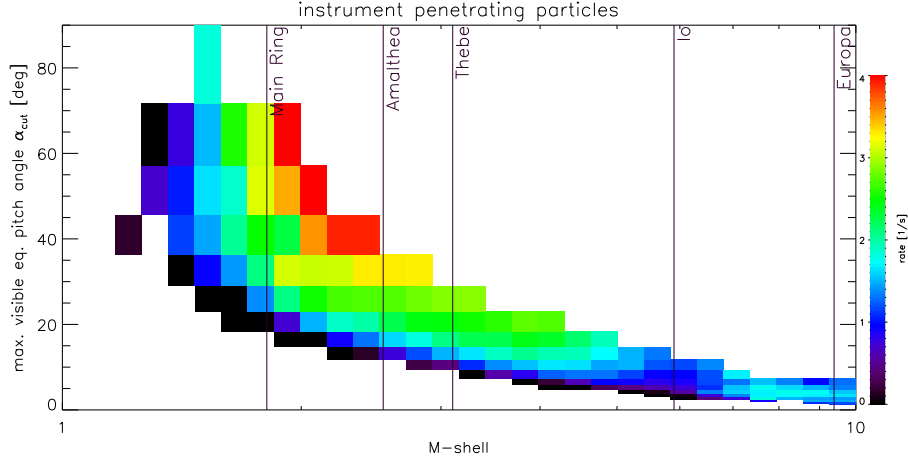
Figure 4. Mission average of penetrating particles as a function of M-shell distance and α_{cut}. The average is logarithmic and requires that each bin includes more than 2 samples. It can be seen that the penetrators appear equatorially trapped and coincide with the middle belts.

3.2 GeV penetrators?

We define "penetrators" as particles that penetrate through the shielding of JEDI, typically from the side, and trigger its detectors without passing through its apertures. (These generally particles are of higher energy than particles that only penetrate the detector and could also be called "penetrators".) These particles contaminate many of JEDI's measurements and are removed from the data that are shown here (Fig. 2). Yet we keep track of the penetrating radiation and show its distribution in Fig. 4.

Penetrators irradiate the instrument from all directions, meaning that the signal is insensitive to the instrument look direction and that we cannot determine their pitch angle. Given that Juno is usually at high latitudes, we can still use α_{cut} to organize the data. The penetrator count rates increase with increasing α_{cut} (decreasing magnetic latitudes). This behavior is consistent with an equatorially trapped population of penetrators. The closer Juno is to the equatorial plane, the more penetrating particles are registered. This suggests that the penetrators are the high energy component of the radiation belts (not transient GCRs or auroral beams).

The highest penetrator intensities are found between $2 \lesssim M \lesssim 4$. There is a sharp decrease at the Main Ring and only very few penetrators are found between ring and planet, where the innermost radiation belt is located *Kollmann et al.* [2017]. The penetrating particles are either > 10MeV electrons or > 3GeV protons, as discussed in Appendix A. We com-

pare the radial profiles of the JEDI penetrators with energetic particle measurements of previous missions (Fig. 1). A strong depletion at the Main Ring is a signature of ions, not of electrons, suggesting that the JEDI penetrators are dominated by $> 3\text{GeV}$ protons, at least around the location of the Main Ring.

4 Innermost belt

4.1 Regions without stable trapping

An initially surprising behavior of the innermost radiation belt is that it does not show during every orbit, which could be interpreted as a result of strong dynamics; however, we argue that this is due to a combination of orbit and magnetic topology.

The left panel of Fig. 5 shows particle intensities along Juno's orbit, projected on the plane of Jupiter's rotational equator. Most orbits in the negative quadrant ($x < 0, y < 0$) show the innermost radiation belt, while it is commonly absent in the positive quadrant ($x > 0, y > 0$) .

The right panel of Fig. 5 shows the magnetic field strength at the magnetic equator, when it can be defined. It turns out there is a region ($x > 0$) where the magnetic field minimum on each field line resides inside the planet (indicated as black diamond symbols on Fig. 5 right panel). No stable trapping is expected on these field lines. We expect vanishing intensities also on neighboring field lines because particles drift around the planet. Such a drift loss cone was already observed in Galileo Probe data [*Nénon et al.*, 2018a]. Here we find that also Juno shows this behavior and JEDI count rates vanish around these regions.

Having a closer look at the data from the single orbits (Fig. 6) we find another reason for the apparent absence of the innermost belt: Sometimes the loss cone fills the entire field of view (Fig. 6, panel C) so that we are unable to sample the equatorially trapped population.

The JRM09+CAN magnetic field model *Connerney et al.* [1981, 2018] is unlike any other previous magnetic field model in the way that it qualitatively predicts regions where we cannot sample the innermost belt. This condition illustrates how valuable a high order field model is for studying radiation close to a planet. Even the most sophisticated model currently available (JRM09 is a degree 10 spherical harmonic) does not provide accurate timing (Fig. 6, panels B and C). Also, there are cases where the qualitative prediction is wrong. Some of the highest intensities found in the innermost radiation belt coincide with times where the field model
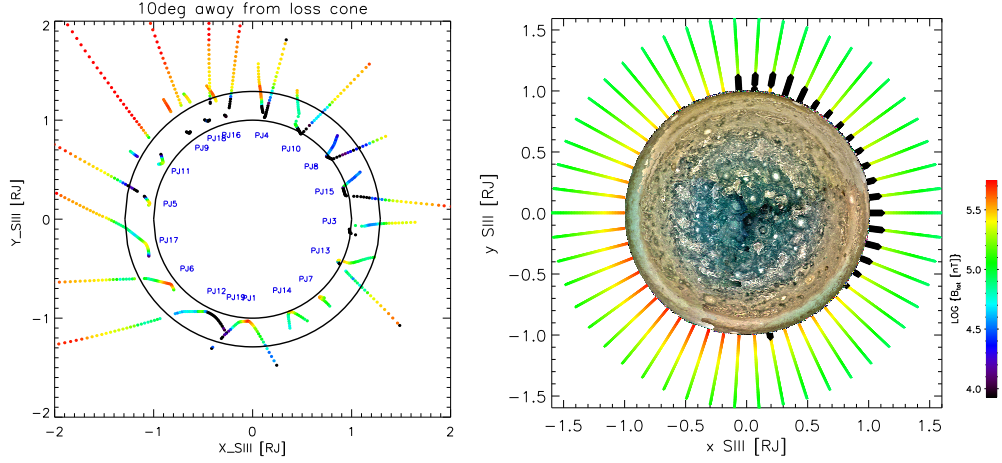
Figure 5. Left panel: JEDI 1MeV total particle intensity (color coded) projected onto the xy plane of the right-handed (east) SIII coordinate system. The inner black circle is Jupiter's surface, the outer black circle is the Main Ring. "PJ" labels indicate the orbit number. It can be seen that the innermost radiation belt (red areas near inner circle) was not always detected, particularly in the positive quadrant. Right panel: Magnetic field strength at the magnetic equator, shown at the location where the respective field line cuts through the rotational equatorial plane. Black diamonds indicate regions in the rotational equatorial plane where no stable magnetic trapping is possible.

does not provide valid M-shells, again because the field model predicts that the minimum field strength along the field line resides inside the planet (panel D). This may well indicate that higher harmonics are necessary to adequately describe the field near the surface of the planet. JRM09 uses but 9 of Juno's 34 Prime mission orbits; a more accurate field model will ultimately be possible with inclusion of many more closely spaced orbits.

The qualitative predictions from the magnetic field model suggest that the innermost radiation belt is not forming and decaying between Juno's 2-month orbits but that particles from the belt only reach the instrument during some orbits.

The pitch angle distribution is very steep near the enormous loss cone found close to the planet (Fig. E.1). Small errors in the pitch angle mapping result in large errors in the expected intensities. Because of these uncertainties we are currently unable to determine if there are more subtle time dependences, for example if the innermost belt is slowly decaying throughout the Juno mission, as we suggest below in Sec. 4.3.
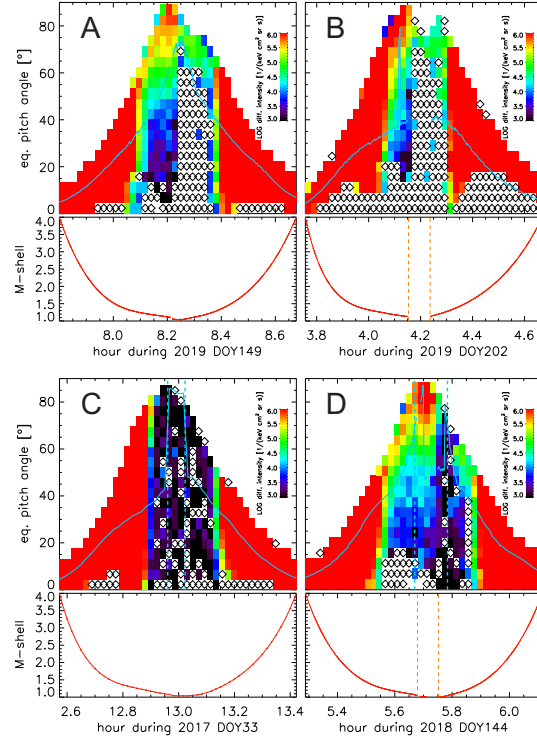
Figure 6. Upper panels: JEDI 80keV total particle intensity (color coded) over equatorial pitch angle (y axis) and time (x axis). Measurements with zero counts are marked with diamond symbols. Equatorial pitch angles that were not accessible from the respective latitude are left white. The blue curve shows the edge of the loss cone in the JRM09+CAN magnetic field model. Lower panels: M-shell calculated in the JRM09+CAN model. Panel A: Well-behaved case where the M-shell is always defined, the loss cone is $\ll 90°$, and the innermost radiation belt is visible. Panel B: No innermost radiation belt visible because no stable trapping exists, indicated by the gap in the M-shell values. Panel C: No innermost radiation belt visible because the loss cone covers the entire field of view. Panel D: The magnetic field model suggests no stable trapping but we find trapped particles, indicating that the model is not perfect.

4.2 Spectral shape

The spectral shape in the innermost radiation belt does show apparent time variability. Some spectra are steadily falling with increasing energy, others show a rise in the hundreds of keV energy range. The larger energy range compared to *Kollmann et al.* [2017] reveals that the spectra fall in the MeV energy range in any case. Figure 3 shows a mission-averaged spectrum as well as one example of a rising spectrum. Given the uncertainties when organizing the data in M-shell and equatorial pitch angle (Sec. 4.1), we currently interpret that variability as an artifact of how we organize the data.

4.3 Possible physics in innermost belt

The distribution of phase space density (PSD) over M-shell can be a useful indicator of the physical processes acting in a radiation belt. The shape of a radial PSD profile can indicate whether the belt may be supplied through local source process of some kind or if can be simply populated by radial transport of particles from large distances, for example through means of radial diffusion [*Lejosne and Kollmann*, 2020]. According to Liouville's theorem, PSD is conserved along trajectories of particles as long as there are no particle sources or losses. We typically observe at all magnetized planets that PSD largely falls toward the respective planet *Paonessa and Cheng* [1985]; *Cheng et al.* [1987, 1992]; *Kollmann et al.* [2011]; *Turner et al.* [2017]. Losses at the planet's surface itself are sufficient to cause falling PSD profiles [*Lejosne and Kollmann*, 2020]. Often losses are enhanced by distributed losses away from the planet, for example from neutral gas tori surrounding it and leading to energy loss [*Clark et al.*, 2014], charge exchange [*Kollmann et al.*, 2011], or waves that scatter particles along the field lines into the atmosphere [*Nénon et al.*, 2018b]. Local increases of the PSD may be caused by a source like the CRAND process [*Cooper and Sturner*, 2018] or the stripping of ENAs [*Kollmann et al.*, 2017] that produce new particles, by sudden radial transport for example through large-scale [*Roussos et al.*, 2018] or small-scale electric fields [*Paranicas et al.*, 2016; *Lejosne et al.*, 2018], or by local acceleration [*Horne and Thorne*, 2003; *Li et al.*, 2014].

Phase space density f (particles per real space volume and volume in momentum space) relates to differential intensity j (particles per time, energy interval, area, and solid angle) as $f = j/p^2$ with the momentum p. Note that at non-relativistic speeds PSD is sometimes defined in velocity instead of momentum space instead, where a different conversion applies. For

our analysis we only use measurements that have the contribution of penetrating particles removed (Appendix C).

The critical part in the calculation of f is not the conversion from j but that f should be for constant first and second adiabatic invariants that are defined as

$$\mu = \frac{E\left(E + 2mc^2\right)}{2mc^2 B} \sin^2 \alpha \tag{2}$$

$$K = \int_{-\lambda_m}^{+\lambda_m} \sqrt{B_m - B}\ \mathrm{d}s \tag{3}$$

E is the kinetic energy of the charged particle, m its rest mass, c the speed of light, B the local magnetic field, B_m the magnetic field at the mirror point (where the particle starts moving back to the equatorial plane), α the local pitch angle between the particle velocity v and the magnetic field, λ the magnetic latitude, and λ_m the latitude of the mirror point. We calculate both invariants in the JRM09+CAN field model, which for K involves a pitch angle dependent integration along the field line.

Ensuring conservation of these invariants is non-trivial as the native measurements of the instrument are at fixed values of E and α. The results are shown in Fig. 7. It can be seen that f decreases toward the planet until $M \approx 1.3$. f is rising for smaller distances for a range of μ and K values.
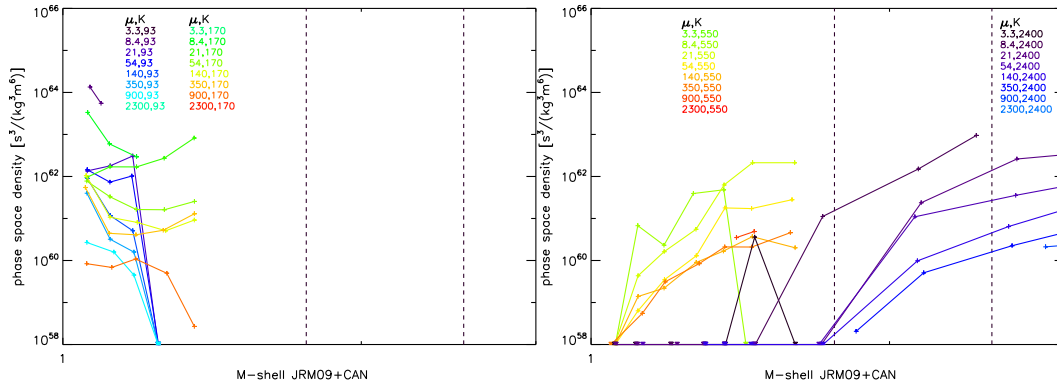

Figure 7. Proton phase space density profiles in and around Jupiter's innermost radiation belt. Different colors and panels are different sets of adiabatic invariants as described in the legend. The units of μ are keV/G and of K are $\sqrt{\mathrm{nT}}R_J$. The left panel shows that PSD rises toward the planet at the smallest distances for several μ and K values, suggesting a non-steady state or local source. The right panel shows falling profiles consistent with inward diffusive transport and losses at the Main Ring and the atmosphere.

A rising PSD profile rules out that the innermost belt is a result of steady inward diffusive transport. The rising PSD profile is consistent with a local source process, supporting the theory of stripped ENAs [*Kollmann et al.*, 2017]. Another possibility is that the belt is supplied by occasional transient but very effective radial transport of some kind. Inferring a local source from a rising PSD profile is only valid for a steady state. The innermost radiation belt is observed to be present whenever the spacecraft is magnetically connected to it. Current uncertainties in mapping M-shells and equatorial pitch angles are too large to reliably study intensity variations (Sec. 4.1). It is possible that the innermost radiation belt is not in steady state but has a slow time dependence on the timescale of years. If true, a rising PSD profile may result from a radial PSD distribution that is initially flat or falling toward the planet and produced for example by a period of efficient radial transport, for example by a transient electric field *Roussos et al.* [2018]; *Lejosne et al.* [2018]. The flat profile can be turned into a rising profile if losses occur mostly at $1.3 \lesssim M \lesssim 1.8$, the region of the ring halo (1.3-1.8 R_J) and Main Ring ($1.8R_J$).

Preliminary analysis suggests the efficiency of ENA stripping is too low to explain the innermost belt but that occasional radial transport plus losses to the rings may explain both the spectra and the PSD distribution [*Kollmann et al.*, 2019, 2020b]. A full analysis will be part of a future publication.

5 Summary

- We unambiguously identify protons and heavy ions for the first time with hundreds of keV in the middle radiation belts ($2 \lesssim M \lesssim 4$), see Fig. 2.
- The middle radiation belts also include a population of particles that penetrate the shielding of the instrument (Fig. 1) that we interpret at GeV protons (Sec. 3.2).
- There are regions above Jupiter's surface where no stable magnetic trapping is possible on individual field lines, see Fig. 5.
- Jupiter's innermost ion belt shows proton spectra that peak in the MeV range (Fig. 3).
- The innermost belt is either populated by a local source or occasional rapid radial transport (Sec. 4.3).

A Identifying particles

JEDI measures ions by detecting their time of flight (TOF) between passing foils near the entrance (start signal) and near the back (stop signal) of the instrument. The particle then enters a solid state detector (SSD) that measures its kinetic energy (energy signal). 2D histograms of counted particle events as a function of energy and TOF are shown in Fig. A.1. TOF allows to calculate the particle's speed. The combination of energy and speed can be used to infer the particle's mass, which should be close to an integer number. Ions with realistic masses line up along a diagonal lines in a TOF vs. energy histogram (Fig. A.1).
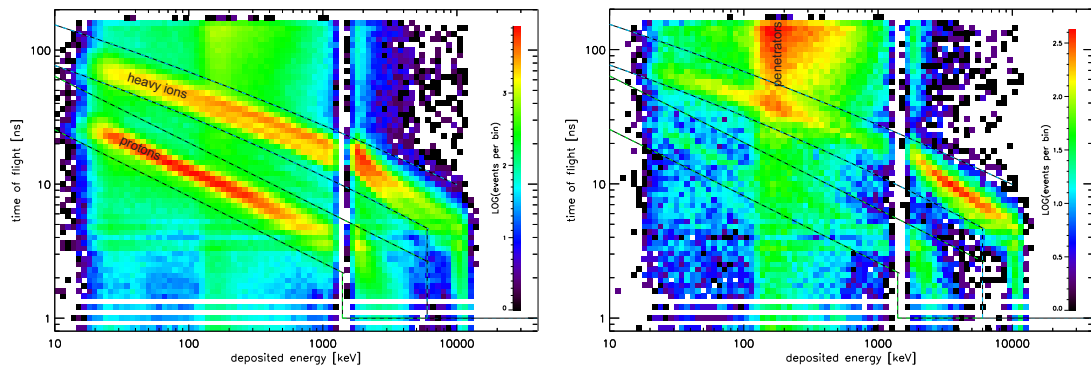
Figure A.1. 2D histogram of JEDI event data. The y axis is the ion time of flight within the instrument. The x axis is the energy deposited within the SSD, which is less than the ambient energy the particle had before entering the instrument. Left: This data shows counts accumulated on days that include closest approaches to Jupiter. It can be seen that most counts form tracks along diagonal lines. The overplotted lines roughly demarcate the regions where protons (lower two lines) and oxygen and sulfur ions (upper two lines) fall. Right: Same as left panel but only for the region of the middle belts. It can be seen that many counts deposit 200keV, indicating that they result from SSD-penetrating protons or electrons (Appendix B.)

Charged particles passing through matter gradually lose their energy because portions of the energy are transferred into ionizing the material. A SSD is able to measure most of the ionization part of the energy loss [*Knoll*, 2000]. If the particle comes to a halt within the SSD, the full particle energy can be calculated. It requires at least > 320keV for electrons and > 8MeV for protons to penetrate through the JEDI's 500μm thick silicon detectors. (Electrons scatter and therefore often effectively traverse more material, requiring higher energies to leave the detector. At 1.2MeV 90% of electrons are stopped within the detector, *Mauk et al.* [2018].) The energy dependence of energy loss per distance [*Berger et al.*, 2005] works out in a way

that > 1.3MeV electrons and > 2.5GeV protons all deposit the same "minimum ionizing" energy of ≈ 200keV energy into the detector. In environments with an abundance of sufficiently energetic particles, there will an artificial spectral peak at ≈ 200keV deposited energy [*Mauk et al.*, 2018]. Heavier ions have a higher minimum ionizing energy and deposit at least 3 times more energy.

> 10MeV electrons, > 60MeV protons, and > 7GeV sulfur ions are energetic enough to penetrate JEDI's shielding and can trigger any of the various signals. Sufficiently energetic particles are relatively rare but can enter the instrument from any direction, different to lower energy particles that have to enter through the narrow apertures. As the coincidence of 3 signals within a constrained time window is required for a valid ion measurement, it is unlikely that 3 independent penetrating particles lead to something that the instrument interprets as a valid ion [*Eckart and Shonka*, 1938]. It does happen however in sufficiently an intense environment, like it exists inward of Io. Such false positive counts can be identified by their mass having non-integer values. Such accidental coincidences are more likely at long TOFs. That such coincidences are indeed happening can be seen in the red area at $\gtrsim 30$ns and ≈ 200keV in the right panel of Fig. A.1.

We keep track of these accidentals through a dump channel (called "TPF0") that keeps track of all particle counts associated with unexpected masses. In high radiation environments, this channel is dominated by penetrators that do not organize well with local pitch angle. In environments without penetrators, this channel is dominated by particles that enter through the aperture but may have masses just outside the allowed boundaries. To distinguish these regimes, we calculate the count rate ratio in the local pitch angle ranges of $80 - 90°$ and $40 - 60°$. For penetrating particles, we require that ratio to be < 2.

The observed penetrators have to result mostly from electrons or protons because heavier ions deposit more than 200keV. The radial dependence of the accidentals (Fig. 1) suggests that they are dominated by protons, at least around the Main Ring (Sec. 3.2).

B Calibrating event data

JEDI's electronics uses different methods to measure the deposited energy. Below 1.2MeV the height of electronic signal from the SSD is used, above that energy the width of the pulse is used. Even the latter method saturates at ≈ 10MeV [*Westlake et al.*, 2019]. Overall, the energy calibration above 1.2MeV is currently not accurate, which is why the slope of the diag-

onals in Fig. A.1 is changing with energy. When analyzing event data we therefore use TOF to determine the ambient particle energy.

When particles penetrate the SSD, the deposited energy typically decreases with increasing ambient energy. A deposited energy value therefore can have 2 TOF values for the same energy: one for particles that stop in the SSD and one for SSD-penetrating particles. Protons with TOF< 1ns penetrate the SSD and are expected to deposit < 3MeV, a combination that we do not observe. This finding suggests that TOF< 1ns events are not meaningful, which is consistent with JEDI's TOF FWHM at MeV energies being ≈ 1ns *Mauk et al.* [2013]. We therefore discard events with TOF< 1ns. This limits the energy range for which we can calculate energy spectra from TOF measurements to ambient energies (in space and before energy loss in the foils) of < 19MeV protons and < 160MeV oxygen.

JEDI provides measurements in different formats. The standard product are rate channels that keep track of all particles but with low energy resolution. Additionally there are event data provided, which only include a subset of the measured particles but have much higher energy resolution. In principle, event data counts can be converted to differential intensity the same way as rate channel counts. For rate channels the intensity j_r calculates as the counts of the respective channel, divided by the energy interval of the channel ΔE, the duration of the chosen time interval ΔT, and the effective geometry factor G [*Mauk et al.*, 2013]. We measure ΔT by finding times where rate data is available and summing over their respective integration times.

We filter the event data with the same criteria as the rate channels (same ΔE energy range, no scattering allowed, etc.). When analyzing event data we sum oxygen and sulfur counts together and calibrate them under the assumption that these heavy ions are all oxygen. We then calibrate the event counts formally the same as for the rate counts. Overall this yields a relative intensity $\widetilde{j}_e$ that describes the shape of the energy spectrum.

The absolute intensity is calculated by multiplying $\widetilde{j}_e$ with the fraction R of particles that are recorded as event data. We calculate R by dividing the intensity j_r from the rate data with $\widetilde{j}_e$. Now we can bin the event data with higher energy resolution and count the events N_e within a smaller energy interval, δE as for the rate channels. The absolute intensity j_e from the event data is then

$$j_e = \frac{N_e R}{\delta E \ \Delta T G} \tag{B.1}$$

We construct mission-averaged event-based spectra by first compiling spectra for the inbound and outbound legs of each orbit. Bins that have less than 10 events are discarded. In the region of the middle belts we discard data around the minimum ionizing energy to avoid considering penetrators (Appendix B). The mission average uses the logarithm of the single spectra and requires that each bin was populated during at least 4 orbits.

C Removing penetrating radiation

Counts that result from penetrating particles (Appendix B) do not organize by pitch angle. Such false counts are approximately the same no matter in which direction the instrument is pointing. This condition means that penetrating particles will lead to similar count rates for all pitch angles, including the loss cone [*Mauk et al.*, 2016]. The loss cone is empty for all energies (Fig. C.1, upper panel) when observing magnetically trapped particles. If intensities inside and outside of the loss cone are found to be similar at a given energy (Fig. C.1, lower panel), this is an indication that the respective measurements may be contaminated. We require that the linear averages of each loss cone is at least a factor of 10 below the linear average of the remaining pitch angle range. If this is not the case or if only data within the loss cone is covered, we remove particles at this energy and species for all pitch angles. This analysis is done energy by energy. We find that high energy measurements are usually more robust because the time of flight is shorter so that there is less chance for accidental coincidence.

The cleaning process used here is meant to be as rigorous as possible. We prefer to have less data over possibly contaminated data. The process also removes times where the loss cone is populated due to a physical reason like auroral acceleration of some kind [*Mauk et al.*, 2018; *Paranicas et al.*, 2018]. If the loss cone is not observable due to spacecraft attitude and orbit, we also remove the data. A comparison between the complete and the cleaned data set can be found in Fig. C.2.

D Averaging over the mission

Figure 2 shows measurements that were cleaned as described in Appendix C and where we averaged the data over the Juno mission. Averaging is complicated by the fact that the channel definitions changed on 2019 DOY 127 UTC 21. Since then JEDI provides heavy ion channels up to 160MeV instead of the earlier used 8 MeV. Before averaging, we therefore need to interpolate the new channel definitions onto the old definitions. No extrapolation is done in our analysis.
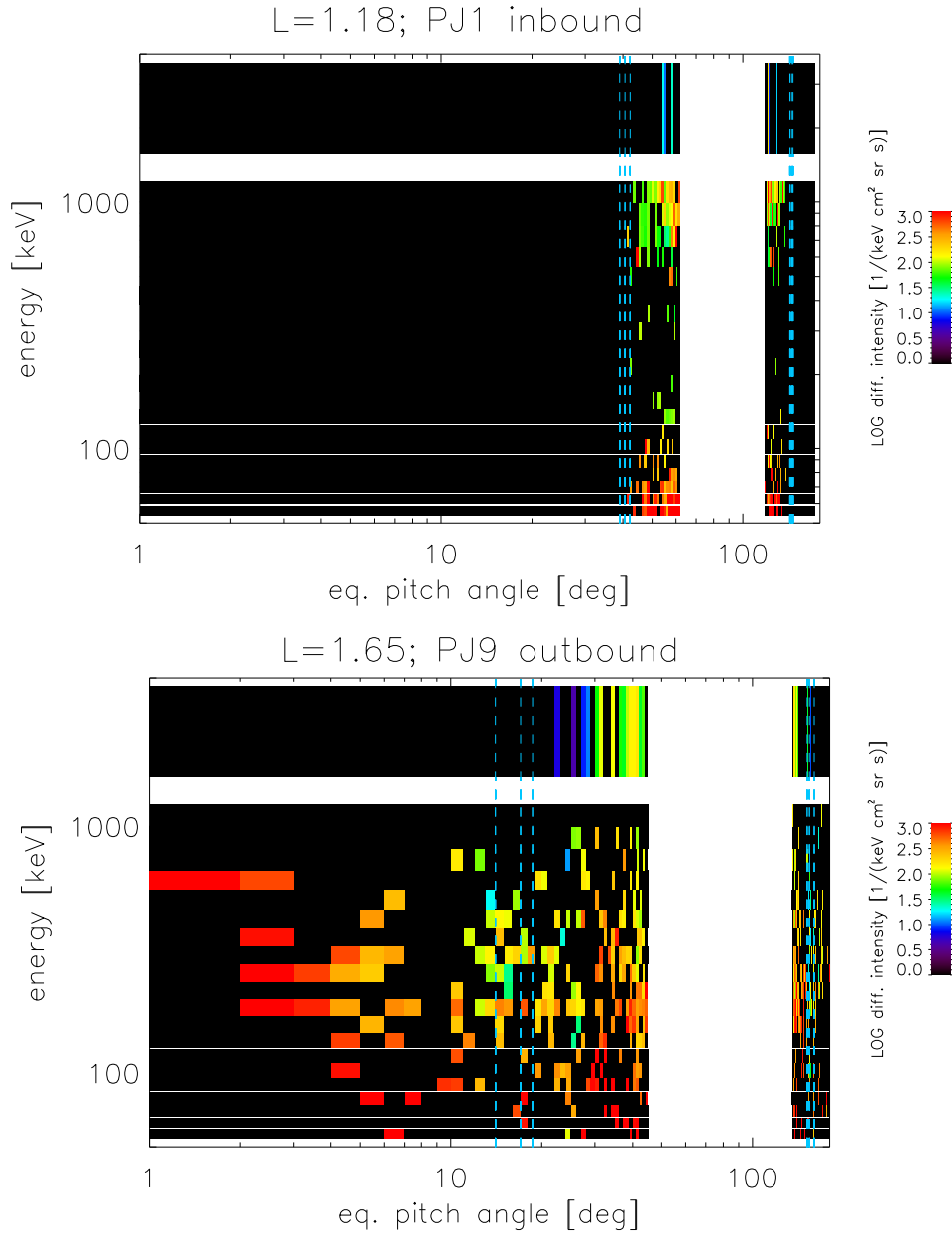
Figure C.1. Proton intensity distribution (color coded) plotted as a function of energy and equatorial pitch angle at two example times. White space oriented vertically corresponds to an equatorial pitch angle range that was not covered because Juno was at too high latitudes. The horizontal white region represents the transition in how energies are measured by JEDI. Blue vertical lines indicate the min, median, and maximum loss cone values during the respective interval for the northern and southern hemisphere. Upper panel: In this example there are no significant intensities inside of the loss cone, consistent with a reliable measurement of trapped protons that enter through the aperture. Lower panel: Significant intensities within the loss cone may indicate that particles penetrate through the instrument shielding and are falsely identified as field-aligned <MeV protons. The higher energies are still reliable in this case.
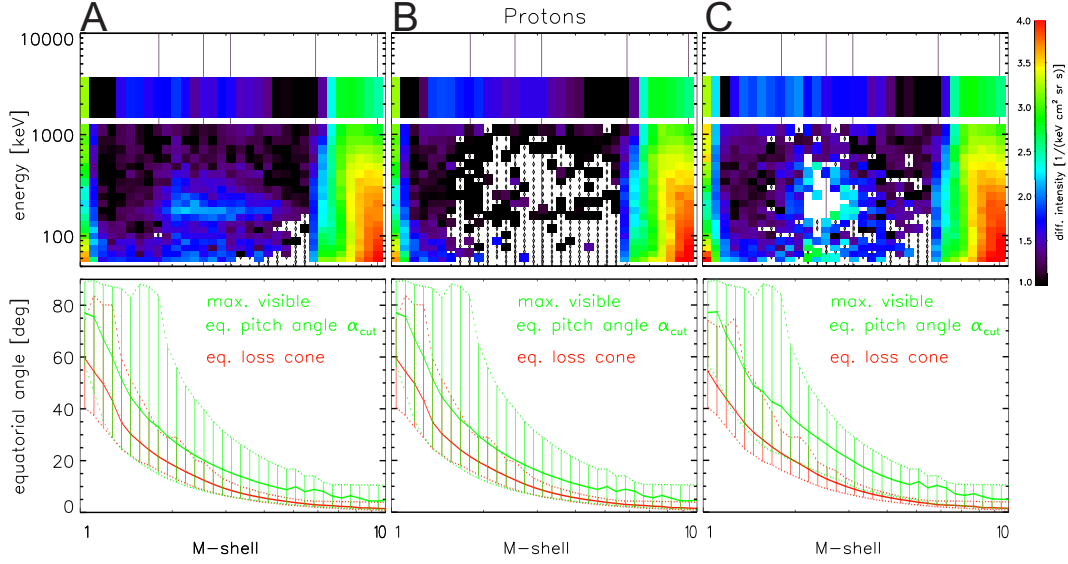
Figure C.2. Mission averaged proton intensities using different filters. Column A: Median of all data, including penetrating particles misidentified as ≈ 200keV protons. Column B: Penetrating particles removed as described in Appendix C. This data set is in parts dominated by measurements in the loss cone that show near zero counts. Column C: Measurements near the loss cone removed as described in Appendix D. This column is identical to what is shown in Fig. 2.

JEDI is able to measure oxygen and sulfur from < 140keV to ≈ 160MeV but can distinguish these two species only from ≈ 300keV to $approx 15$MeV. In order to approximate an oxygen channel spectrum over the full energy range, we determine the O/S count rate ratio at intermediate energies and use it to scale the indistinguishable O+S counts at high and low energies.

The cleaning procedure described in Appendix C removes most samples (in energy and time) of contaminated data but is not perfect due to uncertainties in the magnetic field model. These uncertainties can lead to a misidentification of un/contaminated intervals. We use the median average to avoid that large outliers dominate the result.

The median of the cleaned data shows a large number of zero measurements (see Fig. C.2, column B), likely from data that were taken in the actual loss cone even though the field model suggests otherwise. We therefore add an additional filter before averaging that removes data that were taken close to the modeled (but uncertain) loss cone location. Specifically we require that $\alpha_{cut} - \alpha_l \geq 5°$ and $\alpha_{cut}/\alpha_l \geq 1.5$.

E High latitudes mostly capture loss cone

Figure E.1 shows proton intensities for the inbound and outbound legs of one orbit. It can be seen that only the inbound part of the orbit shows significant intensities in the $2 < M < 4$ range, while the outbound part shows no signatures of the radiation belts in this region. The lower panels in the figure show pitch angles. It can be seen that inbound and outbound differ in the covered equatorial pitch angles α_{cut}. In the pass without radiation belt signature, we find that $\alpha_{cut} \approx \alpha_l$, meaning that JEDI was mostly observing the loss cone, where usually no particles are found (unless some auroral process is involved).

Note that the loss cone in reality is no sharp boundary because also Jupiter's surface has no sharp boundary. Instead there is a steep but still gradual slope in the pitch angle distribution [*Kollmann et al.*, 2017; *Mauk et al.*, 2016]. The smaller the pitch angle, the higher the maximum atmospheric density the particles are exposed to and the lower their intensity is. The pitch angle distribution near the loss cone is therefore a representation of the atmospheric density profile and could be used in the future to constrain it like for Saturn [*Kollmann et al.*, 2018b].

Figure E.1 shows a typical behavior. Orbits without radiation belt signatures have the observational bias of mostly measuring the loss cone. Orbits with radiation belt signature on the other hand may be contaminated.

F Pioneer data

Data from the Pioneer 11/GTT instrument [*Van Allen et al.*, 1974] are available through the planetary data system. These data have the dead time corrections from the original publications [*Van Allen et al.*, 1975] undone and an updated correction applied. Iowa's GTT uses Geiger-Müller counters, the classical example of a detector that has a dead time and is paralyzable. The latter means that for rising true rates the counted rates eventually plateau and then decrease. Detectors A, B, C, and G use identical types of Geiger-Müller tubes with different shielding. Detectors B and C (the latter is shown in Fig. 2) plateau at Jupiter. Laboratory calibration of these tubes showed that the measured rates saturate at different values depending on the radiation. The plateau observed at Jupiter was in-between the plateaus observed in the laboratory. Because dead time corrections are very sensitive to the exact value where saturation occurs, a curve was constructed that fits the in-flight maximum rate at Jupiter. This curve was used to correct the data available in the PDS.
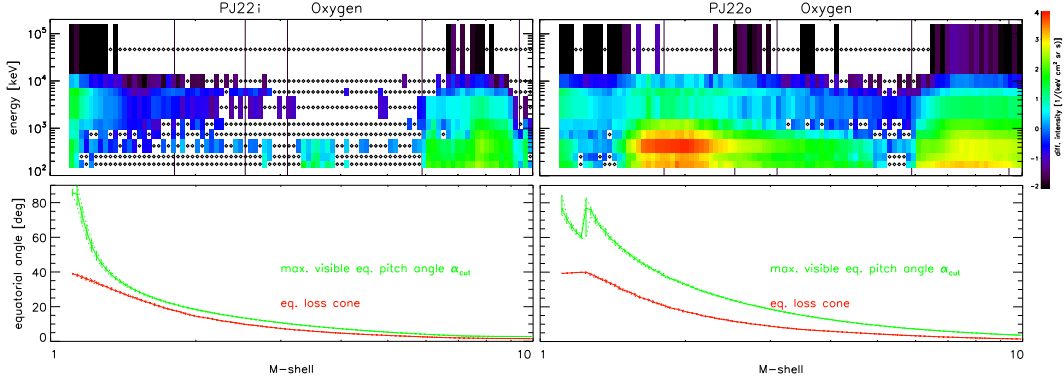
Figure E.1. Upper panels: Intensities (color coded) of 170keV-160MeV oxygen ions as a function of energy (y axis) and M-shell distance to Jupiter (x axis). Diamond signals mark measurements with zero counts. Lower panels: The maximum observable pitch angle α_{cut} at Juno's latitude (green) and the loss cone angle α_l (red). The middle radiation belts at $2 < M < 4$ only show when measurements far from the loss cone are available (right panels). The radiation belts appear absent when the orbital geometry only allows to measure close or within the loss cone (left panels). Data were not cleaned for penetrators and therefore particle energy and species are partly misidentified in the middle radiation belts. See Fig. 2B for cleaned oxygen measurements.

Also this correction is not perfect and sometimes yields > 31MeV electron fluxes that exceed the > 21MeV electron fluxes, which is usually not observed for electrons at Jupiter [*Garrett et al.*, 2016; *Kollmann et al.*, 2018a]. In such cases we revert back to the originally published values where this issue does not exist.

Interactions Node of NASA's Planetary Data System (https://pds-ppi.igpp.ucla.edu/). Galileo Probe count rates were retrieved from *Pehlke* [2000].

References

Baker, D. N., and J. A. van Allen (1976), Energetic electrons in the Jovian magnetosphere, *J. Geophys. Res.*, *81*(4), 617, doi:10.1029/JA081i004p00617.

Berger, M. J., J. S. Coursey, M. A. Zucker, and J. Chang (2005), Stopping-Power and Range Tables for Electrons, Protons, and Helium Ions, The National Institute of Standards and Technology (NIST), http://www.nist.gov/physlab/data/star.

Cheng, A. F., S. M. Krimigis, B. H. Mauk, E. P. Keath, C. G. Maclennan, L. J. Lanzerotti, M. T. Paonessa, and T. P. Armstrong (1987), Energetic ion and electron phase space densities in the magnetosphere of Uranus, *J. Geophys. Res.*, *92*, 15,315–15,328, doi:10.1029/JA092iA13p15315.

Cheng, A. F., C. G. Maclennan, B. H. Mauk, S. M. Krimigis, and L. J. Lanzerotti (1992), Energetic ion phase space densities in Neptune's magnetosphere, *Icarus*, *99*(2), 420–429, doi:10.1016/0019-1035(92)90157-3.

Clark, G., C. Paranicas, D. Santos-Costa, S. Livi, N. Krupp, D. G. Mitchell, E. Roussos, and W.-L. Tseng (2014), Evolution of electron pitch angle distributions across Saturn's middle magnetospheric region from MIMI/LEMMS, *Planet. Space Sci.*, *104*, 18–28, doi:10.1016/j.pss.2014.07.004.

Connerney, J. E. P., M. H. Acuna, and N. F. Ness (1981), Modeling the Jovian current sheet and inner magnetosphere, *J. Geophys. Res.*, *86*, 8370–8384, doi:10.1029/JA086iA10p08370.

Connerney, J. E. P., S. Kotsiaros, R. J. Oliversen, J. R. Espley, J. L. Joergensen, P. S. Joergensen, J. M. G. Merayo, M. Herceg, J. Bloxham, K. M. Moore, S. J. Bolton, and S. M. Levin (2018), A New Model of Jupiter's Magnetic Field From Juno's First Nine Orbits, *Geophys. Res. Lett.*, *45*, 2590–2596, doi:10.1002/2018GL077312.

Cooper, J. F., and S. J. Sturner (2018), Energetic radiation from galactic cosmic ray interactions with saturn's main rings, *J. Geophys. Res.: Space Physics*, *123*, doi:10.1029/2018JA025583.

Eckart, C., and F. R. Shonka (1938), Accidental coincidences in counter circuits, *Phys. Rev.*, *53*, 752–756, doi:10.1103/PhysRev.53.752.

Fillius, R. W., C. E. McIlwain, and A. Mogro-Campero (1975), Radiation Belts of Jupiter: A Second Look, *Science*, *188*(4187), 465–467, doi:10.1126/science.188.4187.465.

Fischer, H. M., E. Pehlke, G. Wibberenz, L. J. Lanzerotti, and J. D. Mihalov (1996), High-Energy Charged Particles in the Innermost Jovian Magnetosphere, *Science*, *272*, 856–858, doi:10.1126/Science.272.5263.856.

Garrett, H. B., M. Kokorowski, S. Kang, R. Evans, and C. M. S. Cohen (2011), The Jovian Equatorial Heavy Ion Radiation, JPL Publication 11-11, `http://hdl.handle.net/2014/41934`.

Garrett, H. B., W. Kim, and R. W. Evans (2016), Updating the Jovian Plasma and Radiation Environments: The Latest Results for 2015, *Journal of Spacecraft and Rockets*, *53*(4), 693–707, doi:10.2514/1.A33510.

Gusev, A. A., G. I. Pugacheva, U. B. Jayanthi, and N. Schuch (2003), Modeling of Low-altitude Quasi-trapped Proton Fluxes at the Equatorial Inner Magnetosphere, *Braz. J. Phys.*, *33*, 775–781.

Horne, R. B., and R. M. Thorne (2003), Relativistic electron acceleration and precipitation during resonant interactions with whistler-mode chorus, *Geophys. Res. Lett.*, *30*, 1527, doi:10.1029/2003GL016973.

Knoll, G. F. (2000), *Radiation detection and measurement*, 3rd ed., John Wiley & Sons, New York, USA.

Kollmann, P., E. Roussos, C. Paranicas, N. Krupp, C. M. Jackman, E. Kirsch, and K.-H. Glassmeier (2011), Energetic particle phase space densities at Saturn: Cassini observations and interpretations, *J. Geophys. Res.*, *116*(A15), A05,222, doi: 10.1029/2010JA016221.

Kollmann, P., C. Paranicas, G. Clark, E. Roussos, A. Lagg, and N. Krupp (2016), The vertical thickness of Jupiter's Europa gas torus from charged particle measurements, *Geophys. Res. Lett.*, *43*, 9425–9433, doi:10.1002/2016GL070326.

Kollmann, P., C. Paranicas, G. Clark, B. H. Mauk, D. K. Haggerty, A. M. Rymer, D. Santos-Costa, J. E. P. Connerney, F. Allegrini, P. Valek, W. S. Kurth, G. R. Gladstone, S. Levin, and S. Bolton (2017), A heavy ion and proton radiation belt inside of jupiter's rings, *Geophys. Res. Lett.*, *44*(11), 5259–5268, doi:10.1002/2017GL073730, 2017GL073730.

Kollmann, P., E. Roussos, C. Paranicas, E. E. Woodfield, B. H. Mauk, G. Clark, D. C. Smith, and J. Vandegriff (2018a), Electron acceleration to MeV energies at Jupiter and

Saturn, *J. Geophys. Res.*, *123*(11), 9110–9129, doi:10.1029/2018JA025639.

Kollmann, P., E. Roussos, A. Kotova, L. Regoli, D. G. Mitchell, J. Carbary, G. Clark, N. Krupp, and C. Paranicas (2018b), Saturn's innermost radiation belt throughout and inward of the D-ring, *Geophys. Res. Lett.*, *45*, doi:10.1029/2018GL077954.

Kollmann, P., B. Mauk, G. B. Clark, C. Paranicas, Q. Nenon, D. K. Haggerty, A. M. Rymer, R. W. Ebert, T. K. Kim, A. Sicard, and J. E. P. Connerney (2019), Jupiter's Innermost Radiation Belts from Juno Measurements, in *AGU Fall Meeting Abstracts*, vol. 2019, pp. SM33C–3210.

Kollmann, P., C. Paranicas, A. Lagg, E. Roussos, Z.-H. Lee-Payne, M. Kusterer, D. Smith, N. Krupp, and J. Vandegriff (2020a), Galileo/EPD user guide, *ESSOAr*, doi:10.1002/essoar.10503620.1, `http://sd-www.jhuapl.edu/Galileo_EPD/userguide/GaliUser_v25C.pdf`.

Kollmann, P., B. Mauk, G. Clark, C. Paranicas, Q. Nenon, Y. Shprits, N. Aseev, R. W. Ebert, T. Kim, E. Roussos, D. Haggerty, A. M. Rymer, A. Sicard, and J. E. P. Connerney (2020b), The innermost ion radiation belts of Jupiter and Saturn, in *EGU General Assembly Conference Abstracts*, EGU General Assembly Conference Abstracts, p. 11829.

Krimigis, S. M., D. G. Mitchell, D. C. Hamilton, N. Krupp, S. Livi, E. C. Roelof, J. Dandouras, T. P. Armstrong, B. H. Mauk, C. Paranicas, P. C. Brandt, S. Bolton, A. F. Cheng, T. Choo, G. Gloeckler, J. Hayes, K. C. Hsieh, W. Ip, S. Jaskulek, E. P. Keath, E. Kirsch, M. Kusterer, A. Lagg, L. J. Lanzerotti, D. LaVallee, J. Manweiler, R. W. McEntire, W. Rasmuss, J. Saur, F. S. Turner, D. J. Williams, and J. Woch (2005), Dynamics of Saturn's Magnetosphere from MIMI During Cassini's Orbital Insertion, *Science*, *307*, 1270–1273, doi:10.1126/Science.1105978.

Krupp, N., V. M. Vasyliunas, J. Woch, A. Lagg, K. K. Khurana, M. G. Kivelson, B. H. Mauk, E. C. Roelof, D. J. Williams, S. M. Krimigis, W. S. Kurth, L. A. Frank, and W. R. Paterson (2004), Dynamics of the Jovian magnetosphere, in *Jupiter. The Planet, Satellites and Magnetosphere*, edited by Bagenal, F., Dowling, T. E., & McKinnon, W. B., pp. 593–616, Cambridge University Press, Cambridge, U.K.

Krupp, N., E. Roussos, P. Kollmann, D. G. Mitchell, C. P. Paranicas, S. M. Krimigis, D. C. Hamilton, M. Hedman, and M. K. Dougherty (2018), Energetic neutral and charged particle measurements in the inner Saturnian magnetosphere during the Grand Finale orbits of Cassini 2016/2017, *Geophys. Res. Lett.*, doi:10.1029/2018GL078096.

Lejosne, S., and P. Kollmann (2020), Radiation Belt Radial Diffusion at Earth and Be-
yond, *Space Sci. Rev.*, *216*(1), 19, doi:10.1007/s11214-020-0642-6.

Lejosne, S., B. S. R. Kunduri, F. S. Mozer, and D. L. Turner (2018), Energetic electron
injections deep into the inner magnetosphere: A result of the subauroral polarization
stream (saps) potential drop, *Geophysical Research Letters*, *45*(9), 3811–3819, doi:
10.1029/2018GL077969.

Li, W., R. M. Thorne, Q. Ma, B. Ni, J. Bortnik, D. N. Baker, H. E. Spence, G. D. Reeves,
S. G. Kanekal, J. C. Green, C. A. Kletzing, W. S. Kurth, G. B. Hospodarsky, J. B.
Blake, J. F. Fennell, and S. G. Claudepierre (2014), Radiation belt electron acceleration
by chorus waves during the 17 March 2013 storm, *Journal of Geophysical Research
(Space Physics)*, *119*(6), 4681–4693, doi:10.1002/2014JA019945.

LLera, K., J. Goldstein, D. J. McComas, and P. W. Valek (2017), Low-altitude emission of
energetic neutral atoms: Multiple interactions and energy loss, *Journal of Geophysical
Research: Space Physics*, *122*(10), 10,203–10,234, doi:10.1002/2017JA024016.

Mauk, B. H., and N. J. Fox (2010), Electron radiation belts of the solar system, *Journal of
Geophysical Research (Space Physics)*, *115*(A12), A12220, doi:10.1029/2010JA015660.

Mauk, B. H., D. G. Mitchell, R. W. McEntire, C. P. Paranicas, E. C. Roelof, D. J.
Williams, S. M. Krimigis, and A. Lagg (2004), Energetic ion characteristics and neu-
tral gas interactions in Jupiter's magnetosphere, *J. Geophys. Res.*, *109*(A18), A09S12,
doi:10.1029/2003JA010270.

Mauk, B. H., D. K. Haggerty, S. E. Jaskulek, C. E. Schlemm, L. E. Brown, S. A.
Cooper, R. S. Gurnee, C. M. Hammock, J. R. Hayes, G. C. Ho, J. C. Hutcheson,
A. D. Jacques, S. Kerem, C. K. Kim, D. G. Mitchell, K. S. Nelson, C. P. Paranicas,
N. Paschalidis, E. Rossano, and M. R. Stokes (2013), The Jupiter Energetic Particle
Detector Instrument (JEDI) Investigation for the Juno Mission, *Space Sci. Rev.*, doi:
10.1007/s11214-013-0025-3.

Mauk, B. H., D. K. Haggerty, C. P. Paranicas, G. Clark, P. Kollmann, A. M. Rymer, L. E.
Brown, S. E. Jaskulek, C. E. Schlemm, C. K. Kim, A. Adriani, S. J. Bolton, F. Bage-
nal, J. E. P. Connerney, G. R. Gladstone, W. S. Kurth, S. M. Levin, D. J. McComas,
and V. P. (2016), Juno observations of energetic charged particles over Jupiter's po-
lar regions: Analysis of mono-and bi-directional electron beams, *Geophys. Res. Lett.*,
accepted, doi:10.1002/2016GL072286.

Mauk, B. H., D. K. Haggerty, C. Paranicas, G. Clark, P. Kollmann, A. M. Rymer, J. M. Peachey, S. J. Bolton, S. M. Levin, A. Adriani, F. Allegrini, F. Bagenal, B. Bonfond, J. E. P. Connerney, R. W. Ebert, G. R. Gladstone, W. S. Kurth, D. J. McComas, D. Ranquist, and P. Valek (2018), Diverse Electron and Ion Acceleration Characteristics Observed Over Jupiter's Main Aurora, *Geophys. Res. Lett.*, *45*, 1277–1285, doi:10.1002/2017GL076901.

Mauk, B. H., G. Clark, F. Allegrini, F. Bagenal, S. J. Bolton, J. E. P. Connerney, D. K. Haggerty, P. Kollmann, D. G. Mitchell, C. P. Paranicas, and A. M. Rymer (2020), Juno Energetic Neutral Atom (ENA) Remote Measurements of Magnetospheric Injection Dynamics in Jupiter's Io Torus Regions, *Journal of Geophysical Research (Space Physics)*, *125*(5), e27964, doi:10.1029/2020JA027964.

Menietti, J. D., Y. Y. Shprits, R. B. Horne, E. E. Woodfield, G. B. Hospodarsky, and D. A. Gurnett (2012), Chorus, ECH, and Z mode emissions observed at Jupiter and Saturn and possible electron acceleration, *Journal of Geophysical Research (Space Physics)*, *117*(A12), A12214, doi:10.1029/2012JA018187.

Nénon, Q., A. Sicard, and S. Bourdarie (2017), A new physical model of the electron radiation belts of Jupiter inside Europa's orbit, *J. Geophys. Res.*, *122*, 5148–5167, doi: 10.1002/2017JA023893.

Nénon, Q., A. Sicard, and P. Caron (2018a), The rings of jupiter as seen by the electron and proton radiation belt model salammbo, *Geophys. Res. Lett.*, (ja), doi: 10.1029/2018GL080157.

Nénon, Q., A. Sicard, P. Kollmann, H. B. Garrett, S. P. A. Sauer, and C. Paranicas (2018b), A Physical Model of the Proton Radiation Belts of Jupiter inside Europa's Orbit, *J. Geophys. Res.*, *123*, 3512–3532, doi:10.1029/2018JA025216.

Nénon, Q., and N. André (2019), Evidence of europa neutral gas torii from energetic sulfur ion measurements, *Geophysical Research Letters*, doi:10.1029/2019GL082200.

Paonessa, M., and A. F. Cheng (1985), A theory of satellite sweeping, *J. Geophys. Res.*, *90*, 3428–3434, doi:10.1029/JA090iA04p03428.

Paranicas, C., M. F. Thomsen, N. Achilleos, M. Andriopoulou, S. V. Badman, G. Hospodarsky, C. M. Jackman, X. Jia, T. Kennelly, K. Khurana, P. Kollmann, N. Krupp, P. Louarn, E. Roussos, and N. Sergis (2016), Effects of radial motion on interchange injections at Saturn, *Icarus*, *264*, 342–351, doi:10.1016/j.icarus.2015.10.002.

Paranicas, C., B. H. Mauk, D. K. Haggerty, G. Clark, P. Kollmann, A. M. Rymer, B. Bon-
    fond, W. R. Dunn, R. W. Ebert, G. R. Gladstone, E. Roussos, N. Krupp, F. Bagenal,
    S. M. Levin, J. E. P. Connerney, and S. J. Bolton (2018), Intervals of Intense Ener-
    getic Electron Beams Over Jupiter's Poles, *J. Geophys. Res.*, *123*, 1989–1999, doi:
    10.1002/2017JA025106.

Pehlke, E. (2000), Teilchenpopulationen in der inneren Jupitermagnetosphäre, Ph.D. thesis,
    Christian-Albrechts-Universität, Kiel, Germany.

Petrov, A. N., O. R. Grigoryan, and N. V. Kuznetsov (2009), Creation of model of quasi-
    trapped proton fluxes below Earth's radiation belt, *Advances in Space Research*, *43*(4),
    654–658, doi:10.1016/j.asr.2008.11.019.

Roussos, E., and P. Kollmann (2020), The radiation belts of Jupiter and Saturn, *arXiv;*
    accepted for AGU book "Magnetospheres in the solar system", arXiv:2006.14682.

Roussos, E., P. Kollmann, N. Krupp, C. Paranicas, K. Dialynas, N. Sergis, D. G. Mitchell,
    D. C. Hamilton, and S. M. Krimigis (2018), Drift-resonant, relativistic electron accel-
    eration at the outer planets: Insights from the response of Saturn's radiation belts to
    magnetospheric storms, *Icarus*, *305*, 160–173, doi:10.1016/j.icarus.2018.01.016.

Roussos, E., O. Allanson, N. André, B. Bertucci, G. Branduardi-Raymont, G. Clark,
    K. Dialynas, I. Dandouras, R. Desai, Y. Futaana, M. Gkioulidou, G. Jones, P. Koll-
    mann, A. Kotova, E. Kronberg, N. Krupp, G. Murakami, Q. Nénon, T. Nordheim,
    B. Palmaerts, C. Plainaki, J. Rae, D. Santos-Costa, T. Sarris, Y. Shprits, A. Sulaiman,
    E. Woodfield, X. Wu, and Z. Yao (2019), The in-situ exploration of Jupiter's radiation
    belts (A White Paper submitted in response to ESA's Voyage 2050 Call), *arXiv e-prints*,
    arXiv:1908.02339.

Turner, D. L., T. P. O'Brien, J. F. Fennell, S. G. Claudepierre, J. B. Blake, A. N. Jaynes,
    D. N. Baker, S. Kanekal, M. Gkioulidou, M. G. Henderson, and G. D. Reeves (2017),
    Investigating the source of near-relativistic and relativistic electrons in earth's inner
    radiation belt, *Journal of Geophysical Research: Space Physics*, *122*(1), 695–710, doi:
    10.1002/2016JA023600.

Valek, P. W., F. Bagenal, R. W. Ebert, F. Allegrini, D. J. McComas, J. R. Szalay, R. J.
    Wilson, S. J. Bolton, and J. E. P. Connerney (2020), Juno in situ observations above the
    jovian equatorial ionosphere, *Geophysical Research Letters*, *47*(12), e2020GL087,623,
    doi:10.1029/2020GL087623, e2020GL087623 2020GL087623.

Van Allen, J. A., D. N. Baker, B. A. Randall, and D. D. Sentman (1974), The magnetosphere of Jupiter as observed with Pioneer 10: 1. Instrument and principal findings, *J. Geophys. Res.*, *79*, 3559, doi:10.1029/JA079i025p03559.

Van Allen, J. A., B. A. Randall, D. N. Baker, C. K. Goertz, D. D. Sentman, M. F. Thomsen, and H. R. Flindt (1975), Pioneer 11 observations of energetic particles in the jovian magnetosphere, *Science*, *188*(4187), 459–462, doi:10.1126/science.188.4187.459.

Westlake, J. H., G. Clark, D. K. Haggerty, S. E. Jaskulek, P. Kollmann, B. H. Mauk, D. G. Mitchell, K. S. Nelson, C. P. Paranicas, and A. M. Rymer (2019), High-Energy (¿10 MeV) Oxygen and Sulfur Ions Observed at Jupiter From Pulse Width Measurements of the JEDI Sensors, *Geophys. Res. Lett.* , *46*(20), 10,959–10,966, doi: 10.1029/2019GL083842.